Caving 2026 – A van As, D Cumming-Potvin & J Wesseloo (eds)

doi:10.36487/ACG_repo/2645_62

Timelapse passive seismic tomography at New Afton C-Zone mine

Erin Bailey [a,*], Yoko Yanagimura [b], Evan Martyniuk [b], Dave Collins [a], Doug Angus [a]

[a] *ESG Solutions, Canada*

[b] *Coeur Mining, Inc, Canada*

Abstract

Passive seismic travel-time tomography is an effective tool for monitoring the initiation and progression of cave growth and tracking the evolution of the stress field of the rock mass. This information is valuable for ground control engineering to better understand how the rock mass is behaving as the cave propagates and identify areas of high stress for risk mitigation. Travel-time tomography maps changes in the P-wave and S-wave travel times to calculate changes in the spatial distribution of P-wave and S-wave velocities. Compared to active source tomography, passive seismic tomography has the benefit of using existing seismic activity to characterise and improve imaging of a subsurface rock body if sufficient ray path coverage exists from source to sensor.

Seismic attenuation tomography is an extension of passive seismic body-wave tomographic analysis that maps changes in attenuation of the higher frequency components of the P-waves and S-waves. Greater attenuation can be interpreted as increased rock damage or the reduction of stress leading to fracture opening.

In this analysis, events and blasts were both used to generate velocity and attenuation tomography results. These are presented and compared to seismicity at monthly intervals for the ongoing development of the New Afton C-Zone cave from undercut blasting to cave initiation and caving propagation. These results are presented alongside and validated by Geo4Sight estimates of the cave shape.

Keywords: *mining, block cave, caving, tomography, attenuation*

1 Introduction

Tomography is an effective tool for characterising the rock mass as it can be done remotely during mining operations using an accurate seismic dataset. Application of travel-time tomography can image spatial and temporal velocity variations throughout an inhomogeneous rock mass and hence infer changes in the rock mass over time. A higher velocity can be equated to more competent rock (e.g. higher bulk modulus) and an increase in velocity can indicate an increase in stress due to the closure of joints, fractures and cracks in the rock mass (e.g. Nur & Simmons 1969). A decrease in velocity, in turn, can be interpreted as a decrease in stress leading to relaxation of the rock mass or damaged rock that can no longer support load. Tomographic analysis performed over time can therefore be used by mining operations to track changes in the stress field and map areas of increased stress and de-stressed rock mass. In block cave mining applications, tomography can be used to map the progression of the cave back and visualise changes in abutment loading conditions, thereby improving hazard assessment in areas where stress changes may accelerate ground response. Kamp et al. (2022) used travel-time tomography to generate low velocity iso-surfaces to be used for cave interpretation around New Afton's B3 cave. Nizkous et al. (2020) combined travel-time tomography with

[*] Corresponding author. Email address: erin.bailey@esgsolutions.com

seismic moment tensor analysis and stress inversion to assess dynamic stress changes during production in a block caving mine.

Attenuation tomography, or Q-tomography, is another tomography method that can use a seismic dataset to map the attenuation field of the rock mass. Attenuation is inversely proportional to a quality factor, Q, such that higher Q values are interpreted as less attenuating rock and lower Q values are interpreted as more attenuating rock. Similar to travel-time tomography, the attenuation tomography method can be applied to locate areas of contrasting rock properties. Reitbrock (2001) and Eberhart-Phillips and Chadwick (2002) demonstrated the use of attenuation tomography to delineate known geological structures around faults. Barthwal et al. (2019) used attenuation tomography to map mined cavities in an underground mine and found correlation between velocity and attenuation where more competent, faster rock is less attenuating compared to more fractured and slower rock. Krauß et al. (2014) compared travel-time tomography to attenuation tomography around an underground excavation and found that attenuation tomography was more sensitive to changes in the rock mass compared to velocity tomography, suggesting attenuation tomography may be superior in some applications.

However, attenuation tomography is generally employed less often than travel-time tomography because it requires use of the full waveform and not just the P-wave and S-wave arrival times. Waveforms can be heavily impacted by signal quality and analysis is limited by the bandwidth of the sensors used in recording the seismicity. To help remove station effects on amplitude, Romero et al. (1997) employed the use of an averaged signal across multiple stations and used a relative attenuation. Other forms of attenuation other than so-called micro-scale anelastic attenuation, such as scattering seismic energy, can also impact the observed attenuation at a sensor. Watanabe & Sassa (1996) suggest using the travel-time tomography velocity field to adjust the ray paths used for attenuation tomography to account for these velocity effects on the wave amplitude.

In this analysis, a method employed by Scherbaum (1990) is applied to image the attenuation field around New Afton's C-Zone block cave mine. This method relies on the accurate recording of the high-frequency roll-off of an event as well as accurate determination of the corner frequency and spectral plateau. The frequency range necessary to do this will vary depending on the size of the event, with smaller events having higher corner frequencies and larger events having lower corner frequencies. At New Afton, a variety of sensors have been installed that cover a combined frequency range of 4.5–2,500 Hz. This combined frequency bandwidth allows for accurate characterisation of the frequency content for moment magnitudes in the range of −2.5 to +2.5 Mw.

Attenuation tomography will be presented alongside traditional travel-time tomography results for a comparison of the methods in reference to block cave monitoring. Travel-time and attenuation tomography are both applied for a range of time windows, and the results are evaluated and compared to improve the understanding of cave propagation in C-Zone and to assess zones of elevated stress.

2 Methodology

2.1 Geology and 1D velocity determination

New Afton’s C-Zone mining development is located roughly 1.1 km underground, and 370 m below the existing B3 cave. Figure 1 shows the location of the C-Zone relative to the B3 cave, as well as the East and West caves and the historical Afton pit.

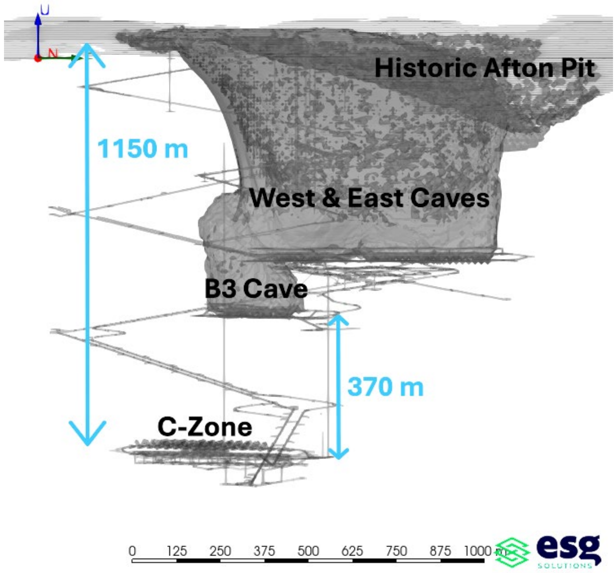

Figure 1 View looking north of the New Afton mining complex

Figure 2 shows the plan view of different lithologies observed at the C-Zone extraction level, along with the numerous faults (black traces) that transect the deposit. The extraction footprint and overlying block cave is hosted within fragmental and crystalline volcanic rocks or 'BXF' that surround monzonite and diorite intrusions (New Gold Inc. 2020 NI 43-101 Report). To the south of the footprint, the deposit is terminated by an ultramafic picrite flow that is significantly less competent than the surrounding rock. South of the picrite, conglomerate of the Jurassic Ashcroft Formation has been projected. The SWPCTC fault (Southwest picrite contact) is modelled at this contact between picrite and the sedimentary rocks. Around this contact heightened seismic activity occurs, associated with more frequent, large events.

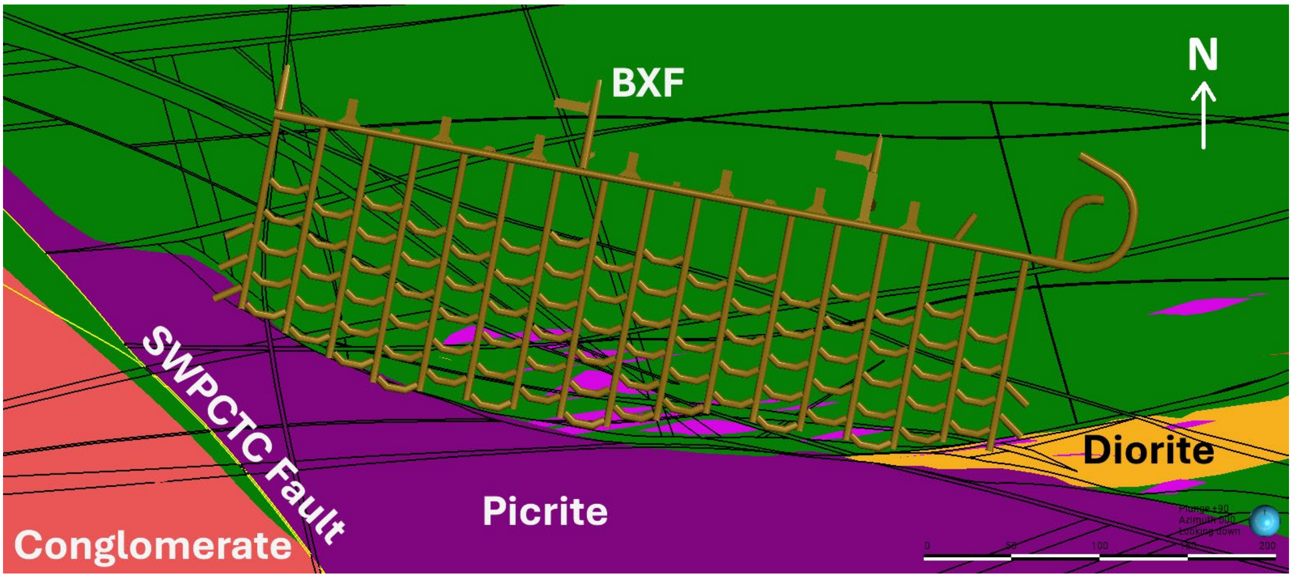

Figure 2 Different rock domains surrounding the C-Zone extraction levels. Seismicity produced by the SWPCTC fault was included in the tomographic analysis

The average in situ P-wave and S-wave velocity around the C-Zone was determined using surveyed blasting locations that occurred prior to cave initiation. Using the differences in blast arrival times and distances to seismic sensors, the average P-wave velocity was estimated to be 5,420 (±130) m/s and the average S-wave velocity was estimated to be 2,980 (±160) m/s. The resulting homogeneous (1D) velocity model produced an estimated location accuracy of 25 m for the known blast locations. These blasts were located along the

C-Zone undercut and will represent the location accuracy along the undercut only. The location estimates for seismic events above the C-Zone are expected to be more accurate because they are more centrally located in the array. Furthermore, events have clearer S-wave arrivals than blasts, which can improve the location accuracy compared to blasts. The estimated P-wave velocity for the C-Zone is slightly higher than the reported velocity of 5,190 m/s for the B3 cave (Kamp et al. 2022), whereas the S-wave velocity is within uncertainty of the reported velocity of 3,000 m/s for the B3 cave.

2.2 Seismic system

The seismic system for monitoring the C-Zone cave is shown in Figure 3. It consists of 3 uniaxial 1V/g accelerometers (frequency range of 50–2,500 Hz), 6 uniaxial 15 Hz geophones and 10 triaxial 15 Hz geophones (frequency range of 15–1,000 Hz), and 3 triaxial 4.5 Hz geophones (frequency range of 4.5–500 Hz). Some of these sensors were installed previously to monitor the B3 cave. Three of the uniaxial sensors (a 15 Hz geophone and 2 uniaxial accelerometers) are located directly above the C-Zone undercut and will be damaged during cave propagation, serving as an additional indicator of cave growth. No sensors could be installed to the south of the C-Zone or the B3 cave due to the poor rock quality of the picrite rock.

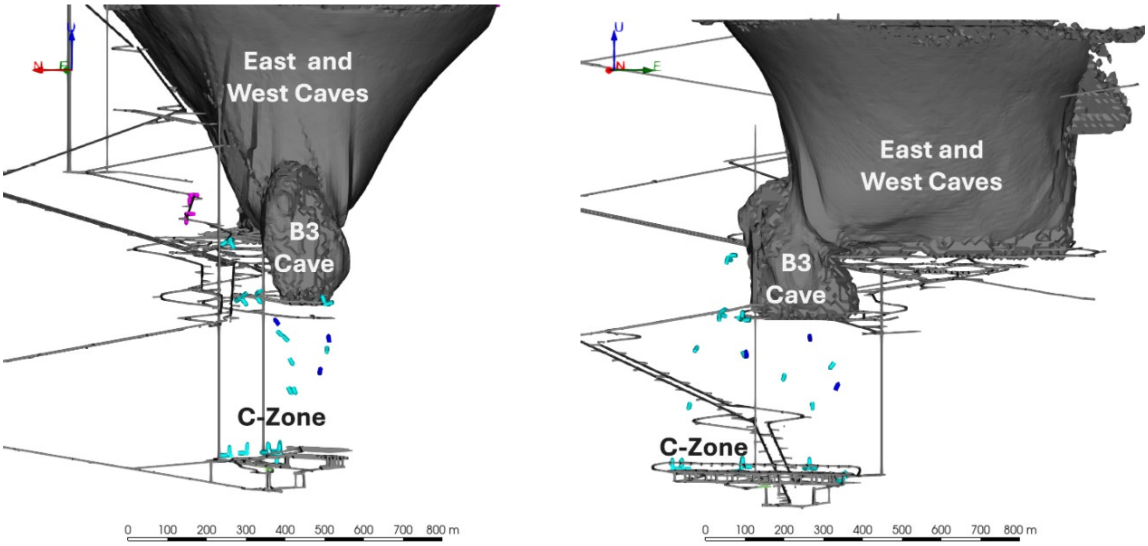

(a) (b)

Figure 3 The C-Zone seismic system, where 15 Hz geophones are coloured light blue, 30V/g accelerometers are coloured dark blue, and 4.5 Hz sensors are coloured pink. Not visible is a surface 4.5 Hz sensor located roughly 1.5 km southeast of the B3 cave. (a) View angle azimuth of 100°; (b) View angle azimuth of 10°

2.3 Data

Monthly tomography analysis was performed throughout 2025 using blast and event data. This dataset uses locations computed from robust and calibrated automatic processing algorithms followed by manual quality control. Manual quality control includes a review of blast and event locations with higher estimated location error and locations that appear to be scattered. Additional data quality thresholds were applied to select a subset of the highest-quality locations for each monthly analysis. This involved excluding waveforms with poor signal-to-noise on most of the sensors and excluding locations with a higher uncertainty, as represented by high P-wave and S-wave residual time differences.

A total of 144,364 events and 4,892 blasts were used in this analysis. Table 1 gives a breakdown of the data used for each monthly tomography interval. The moment magnitude of the data ranges from approximately −2.5 to +2.5 Mw, with the smallest magnitude events recorded above the north side of the C-Zone undercut.

Table 1 Monthly tomographic data

Month (2025)	Number of events	Number of blasts	Total number used
January	1,609	528	2,137
February	3,450	565	4,015
March	6,152	627	6,779
April	3,901	478	4,379
May	13,442	510	13,952
June	9,990	321	10,311
July	10,907	285	11,192
August	9,916	416	10,332
September	11,627	329	11,956
October	16,250	357	16,607
November	14,324	308	14,632
December	42,796	168	42,964

Figure 4 shows all 12 months of data throughout 2025. Some noteworthy observations from these images are the lack of seismicity directly south of the C-Zone caving area and the seismicity observed further south of the C-Zone along the SWPCTC fault structure.

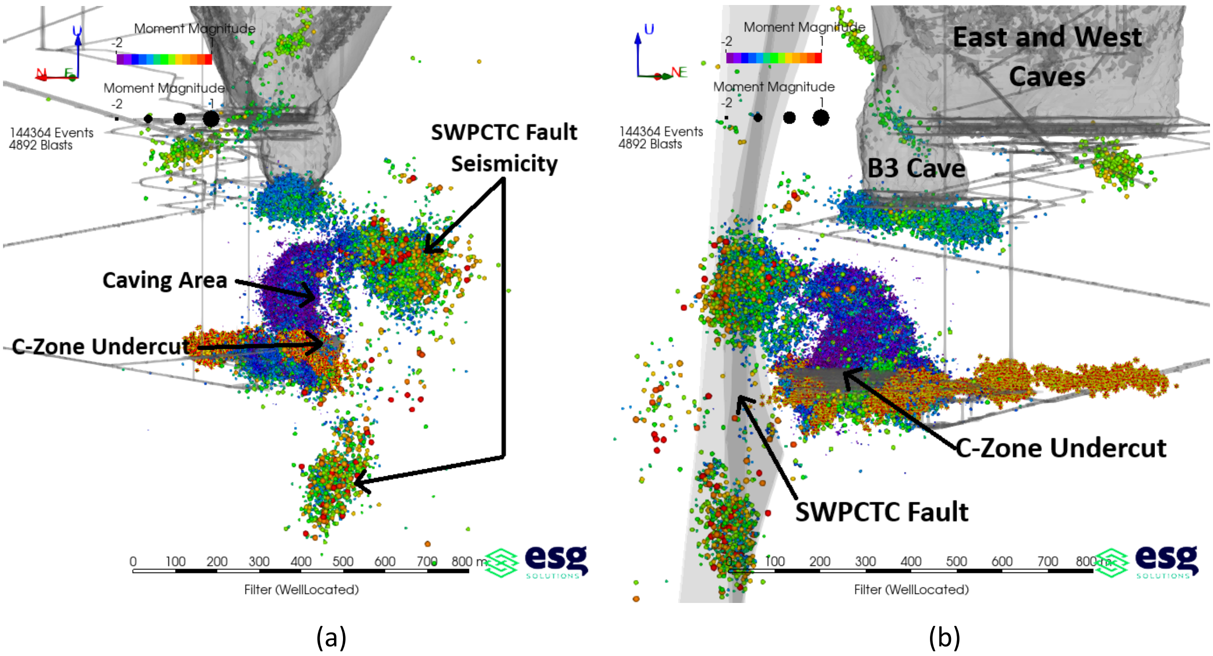

Figure 4 12 months of seismicity used for this tomography analysis. (a) Azimuthal angle of 100° from north; (b) Azimuthal angle of 10° from north

It is thought that the softer picrite rock mass on the south side of the C-Zone mining area is undergoing aseismic deformation. In contrast, the north side of the C-Zone in the BXF rock mass is hard and brittle, with the capacity to store energy, resulting in ample seismicity with moment magnitudes as small as −2.5 Mw being recorded by the seismic system.

The lack of seismicity on the south side combined with absence of installed sensors on the south side poses a challenge for tomographic analysis, which relies on ray path coverage from source to sensor through the area of interest.

The seismicity located further south, away from the C-Zone mining area, is located along a known fault structure (SWPCTC fault) that runs between the picrite and conglomerate rock domains. Seismicity was consistently recorded along this structure throughout the entire analysis period. The moment magnitude range of the seismicity recorded along this structure was between −1.8 and +2.3 Mw. The seismicity has been located predominantly in 2 clusters to the southwest of the C-Zone at depths of 925 m and 1,460 m below surface. The seismicity associated with the SWPCTC fault suggests that the array is capable of detecting seismicity on the south side of C-Zone. This indicates that the relative absence of recorded seismicity south of the C-Zone cave is likely to reflect geological controls than a limitation of the array.

2.4 Travel-time tomography methodology

The travel-time tomographic method used in this analysis is extended from Crowley et al. (2015). The method uses a modified simultaneous iterative reconstruction technique (SIRT). It involves selecting a volume of interest for tomographic analysis, gridding that volume, and then iteratively adjusting the velocity estimate to minimise the time residuals between expected waveform arrivals and the picked waveform arrivals. This method also sets a constraint on the minimum and maximum velocity that can be determined in each grid volume. This constraint prevents the velocity estimates from varying too widely within each grid block and allows the variance in estimates to be used to assess the robustness of the solution. Grid volumes with few ray paths or poorly constrained velocity estimates can then be identified and excluded from the visible field. This precludes the need for a separate resolution (checkerboard) test and makes visualisation of the data confidence easier.

The New Afton volume was gridded into 50 × 50 × 50 m^3 grid blocks. This is the same grid cell size used in the previous tomography analysis around the B3 cave (Kamp et al. 2022). This grid size was chosen based on ray path coverage (the need for a sufficient number of ray paths through each grid block) as well as the wavelength of recorded frequencies, where tomography will not be able to resolve heterogeneities that are smaller than the seismic wavelength. With a P-wave velocity of 5,420 m/s, a 50 m grid spacing assumes that all data have recorded frequency content above 100 Hz. This is a valid assumption for this dataset, which has an average P-wave corner frequency of roughly 500 Hz.

The starting velocity used for the monthly tomographic analysis was set to the initial 1D velocity model determined for the C-Zone site (Vp = 5,420 m/s and Vs = 2,980 m/s). The internal constraint set on the velocity within each grid block was ±50% of this starting velocity model. From the tomographic inversion, only results from grid cells that have variance <50% are shown.

2.5 Attenuation tomography methodology

The attenuation of a rock mass can be characterised by seismic energy E loss and is defined by the inverse of a dimensionless quality factor Q. The parameter Q is defined as the loss of energy ΔE per oscillation cycle:

$$Q = 2\pi E/\Delta E. \quad (1)$$

Attenuation tomographic analysis estimates the Q parameter across a volume of rock mass following the methodology described by Scherbaum (1990), where the observed amplitude spectrum from an event j at a sensor k is described by:

$$A_{kj}(f) = I_k(f) \cdot R_j(f) \cdot S_j(f) \cdot e^{-\pi \cdot f \cdot \tau_{kj}}. \quad (2)$$

where $I_k(f)$ is the frequency dependent sensor response, $R_j(f)$ is the local site effect on amplitude and $S_j(f)$ is the event source spectrum amplitude.

The remaining term describes the absorption along the ray path from source to sensor, where τ_{kj} is the cumulative effect of attenuation along the ray path, and V is the velocity of the wave:

$$\tau_{kj} = \int_{path} dr/(Q \cdot V). \tag{3}$$

Assuming a Brune source model for $S_j(f)$ (Brune 1970), the amplitude of a particular frequency f at sensor k for an event j with corner frequency f_{cj} and spectral plateau Ω_{oj} can be described as:

$$A_{kj}(f) = 2\pi f \Omega_{oj} \cdot \frac{f_{cj}^2}{f_{cj}^2 + f^2} I_k(f) \cdot R_j(f) \cdot e^{-\pi \cdot f \cdot \tau_{kj}}. \tag{4}$$

Similar to velocity tomography, attenuation tomography takes a volume of interest and grids the volume into discrete cells. Then, taking observed parameters (in this case, $\ln(A_{kj}(f))$), the algorithm inverts for the Q values in each grid cell using multiple ray paths through the cell.

The 50 × 50 × 50 m^3 gridding used is the same as in the travel-time tomography. The same modified SIRT method is used in the inversion. The starting estimate of the P-wave attenuation parameter Qp was set to be 150 and the internal constraint on Qp was set to ±50% of the starting value. Similar to travel-time tomography, only grid cells with well constrained Qp estimates (internal variance <50%) are shown.

Mild Gaussian smoothing is applied to both the P-wave and Q-tomography fields to aid with interpretation of general trends. This can cause some artifacts along the edge of the usable field and is visible as a low velocity or low Q area along the edge of the fields.

3 Result

3.1 P-wave velocity tomography

Figure 5 shows the results of the P-wave velocity tomography at monthly intervals throughout 2025. For comparison, Figure 6 shows the seismicity above the C-Zone at the same monthly intervals.

The timelapse tomography displays an initial lower velocity zone around the undercut level compared to the higher velocity zone mid-way between the C-Zone undercut and the B3 undercut. At this time, undercut blasting was already under way and the rock mass in the vicinity of the undercut level is interpreted to be damaged. However, looking at the seismicity above the C-Zone in January, the caving process had not yet initiated.

Between January and May, the velocity field is relatively stable. Comparing to the seismicity shown in Figure 6, the seismicity is occurring in similar areas throughout January and April. In May, the rate of seismicity increased above the undercut. In June, velocity above the undercut decreased noticeably and by July, a low velocity zone began to develop. From July to November, the west abutment showed several cycles of decreasing and increasing velocity, suggesting alternating periods of stress relaxation and reloading. The response occurred as the seismogenic zone shown in Figure 6 migrated upwards on the northwest side of the undercut. In contrast, both the velocity field and the seismicity on the east side of the C-Zone remain relatively static during this period. In October the seismogenic zone began to migrate upwards on the east side. In November, a sustained cluster that had been present over the northeast side of the undercut since May dissipated and was absent entirely in December. This coincided with a sudden expansion of the low velocity zone eastwards seen in the November tomographic window. This suggests cave initiation on the east side between October and November. The December tomography shows additional westward expansion of the low velocity zone on the west side and an increase in velocity in the east and west abutments, suggesting stress loading throughout December. At the same time, the velocity decreases around the apex of the C-Zone cave and beneath the B3 cave.

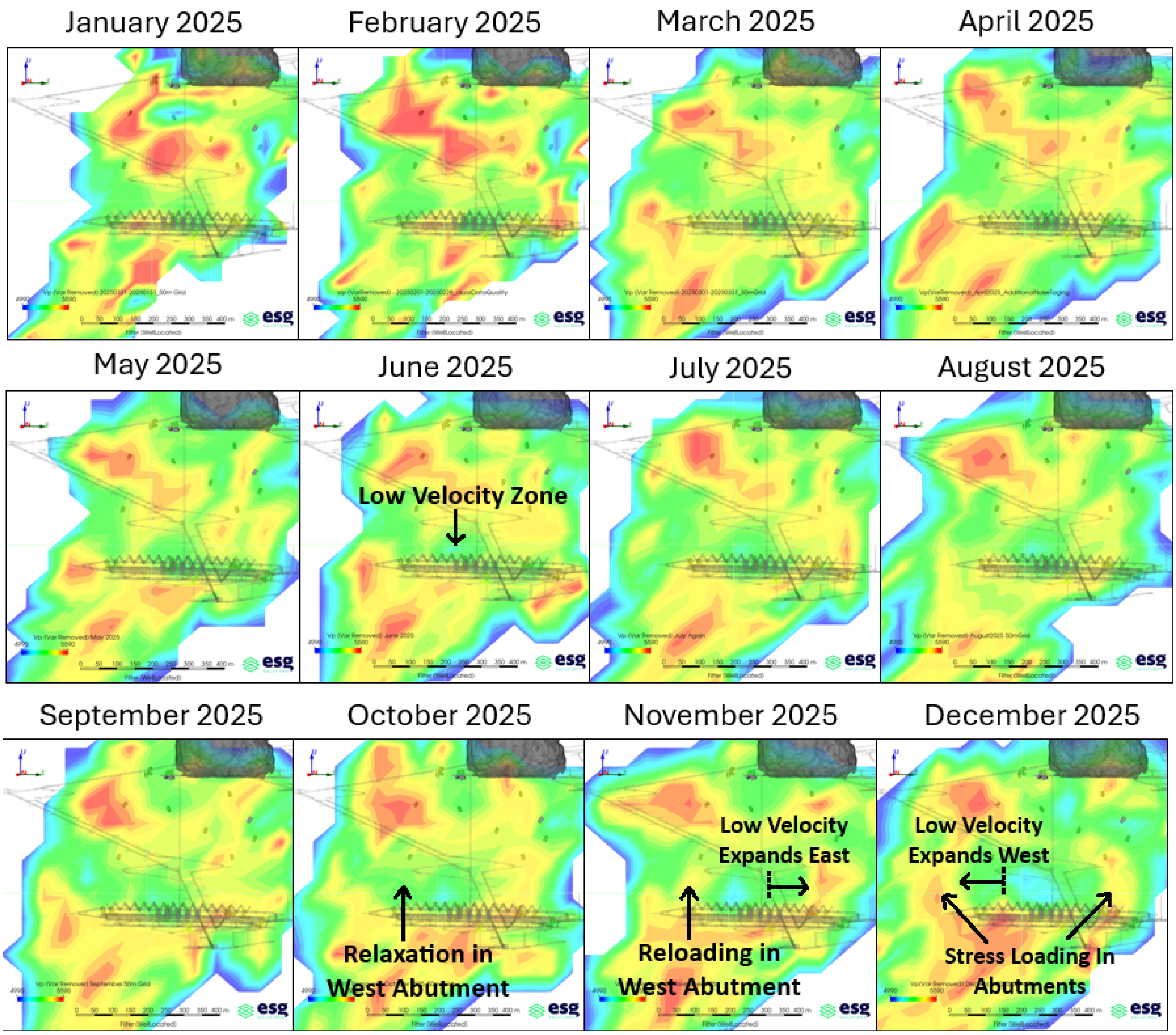

Figure 5 **Monthly P-wave velocity tomographic results from January to December 2025. The view angle is aligned perpendicular to the long edge of the C-Zone undercut at an azimuthal angle of 10° from north. The cutting plane for all images is the same and is aligned parallel to the long edge of the undercut with an azimuthal angle of 100° and runs central to the undercut**

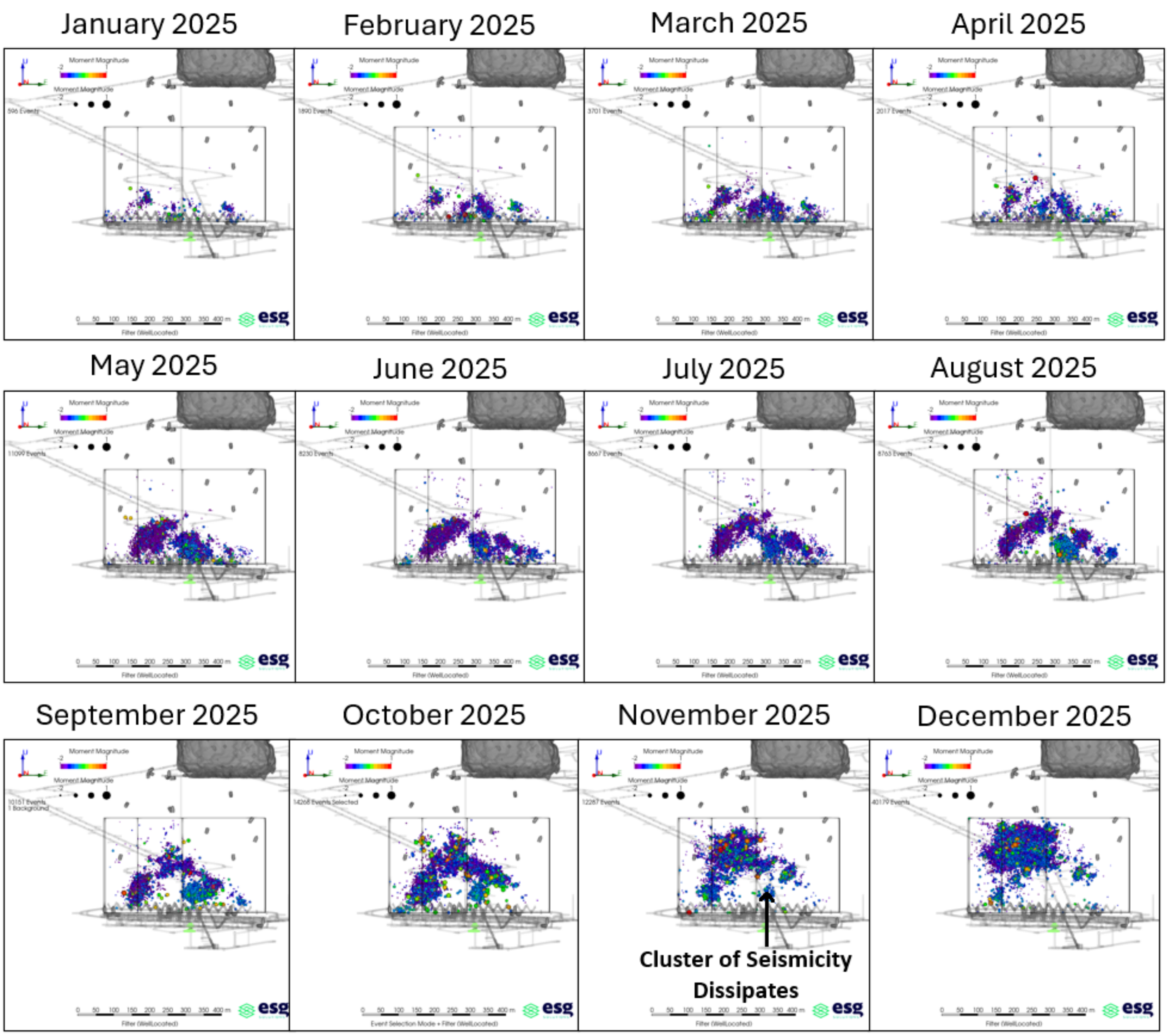

Figure 6 Seismicity above the C-Zone from January 2025 through December 2025. The view angle is aligned perpendicular to the long edge of the C-Zone undercut at an azimuthal angle of 10° from north

Figure 7(a) is a zoomed-in image of the C-Zone seismicity in December along with a conservative estimate of the C-Zone cave shape based on Geo4Sight and the December P-wave velocity field. The tomographic field shows good agreement with the estimated cave shape on the east side of the cave, with a low velocity zone following the shape of the cave. The low velocity zone on the west side however extends higher than the estimated cave shape. Figure 7(b) shows the velocity difference field between December 2025 and January 2025. This field shows good agreement with the estimated cave shape and shows that the P-wave velocity on the west side of the cave has increased since January, despite having a lower velocity than the surrounding rock. These images also indicate that although the seismicity is occurring in a relatively faster velocity rock mass, the P-wave velocity of this rock mass has decreased over time. This is consistent with the intact seismogenic zone beginning to yield.

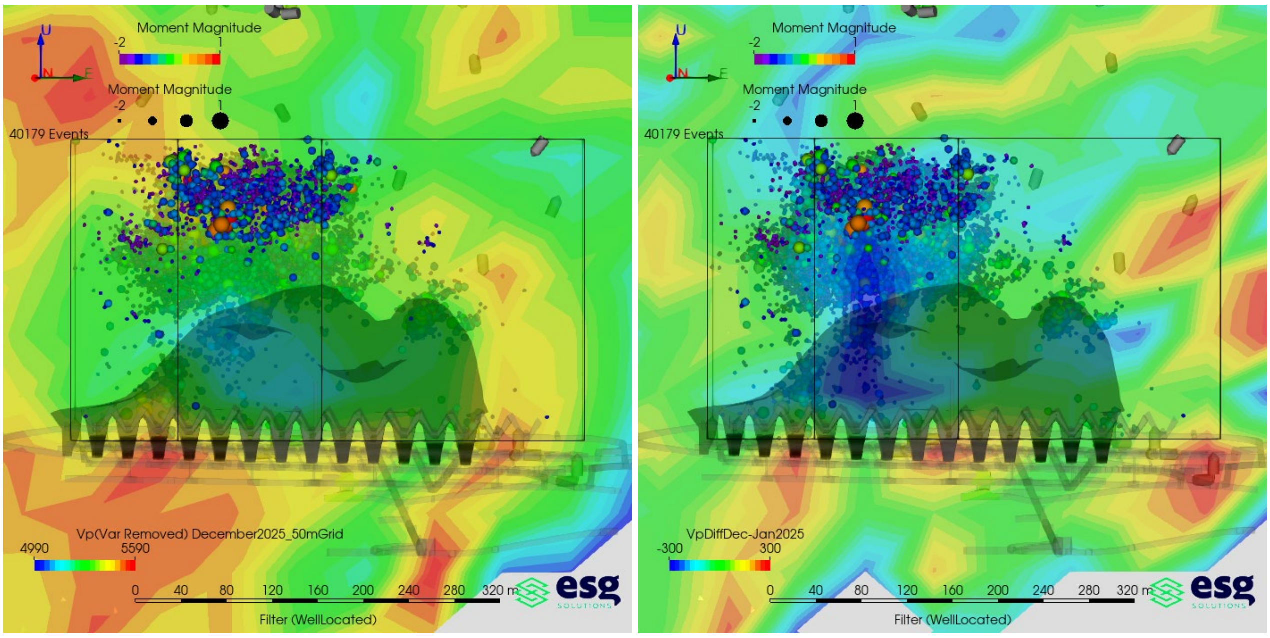

(a) (b)

Figure 7 (a) P-wave velocity field for December 2025; (b) P-wave difference field showing the change in velocity from January to December 2025. The estimated cave shape from Geo4Sight obtained at the start of January 2026 and the December 2025 seismicity above the C-Zone are superimposed on these images

3.2 Attenuation tomography

Similar to travel-time tomography, attenuation tomography fields were generated at monthly intervals, consistent with the seismicity and velocity tomography results. Figure 8 shows the results of the attenuation tomographic analysis with cutting planes positioned in the same location as the P-wave tomography fields in Figure 5. The results of the attenuation tomography show that the observable field, defined by variance below 50%, is smaller than the P-wave velocity field. Given that the attenuation tomography uses the same internal constraints, this suggests that greater uncertainty is associated with the attenuation parameter for the same number of ray paths in a grid volume. For the months of January, April, August and September, the field does not fully extend across the entire C-Zone at the undercut elevation and west side. The months of April and August have high Q value estimates in the expected caving zone compared to other months; this requires further investigation.

February and March show the expected lower Q values around the mid-point of the undercut, extending westward in May. The observed expansion of the low Q zone occurs prior to the observed expansion of the lower velocity zone westwards. October shows an expansion of the low Q zone eastwards, again prior to the observed expansion of the low velocity zone eastwards in November. This supports the idea that the Q value may be a more sensitive and timely indicator to changes occurring in the rock mass, as previously reported by Krauß et al. (2014). This may be because the Q value is inherently using more information from the seismic wave compared to velocity, which only requires arrival times.

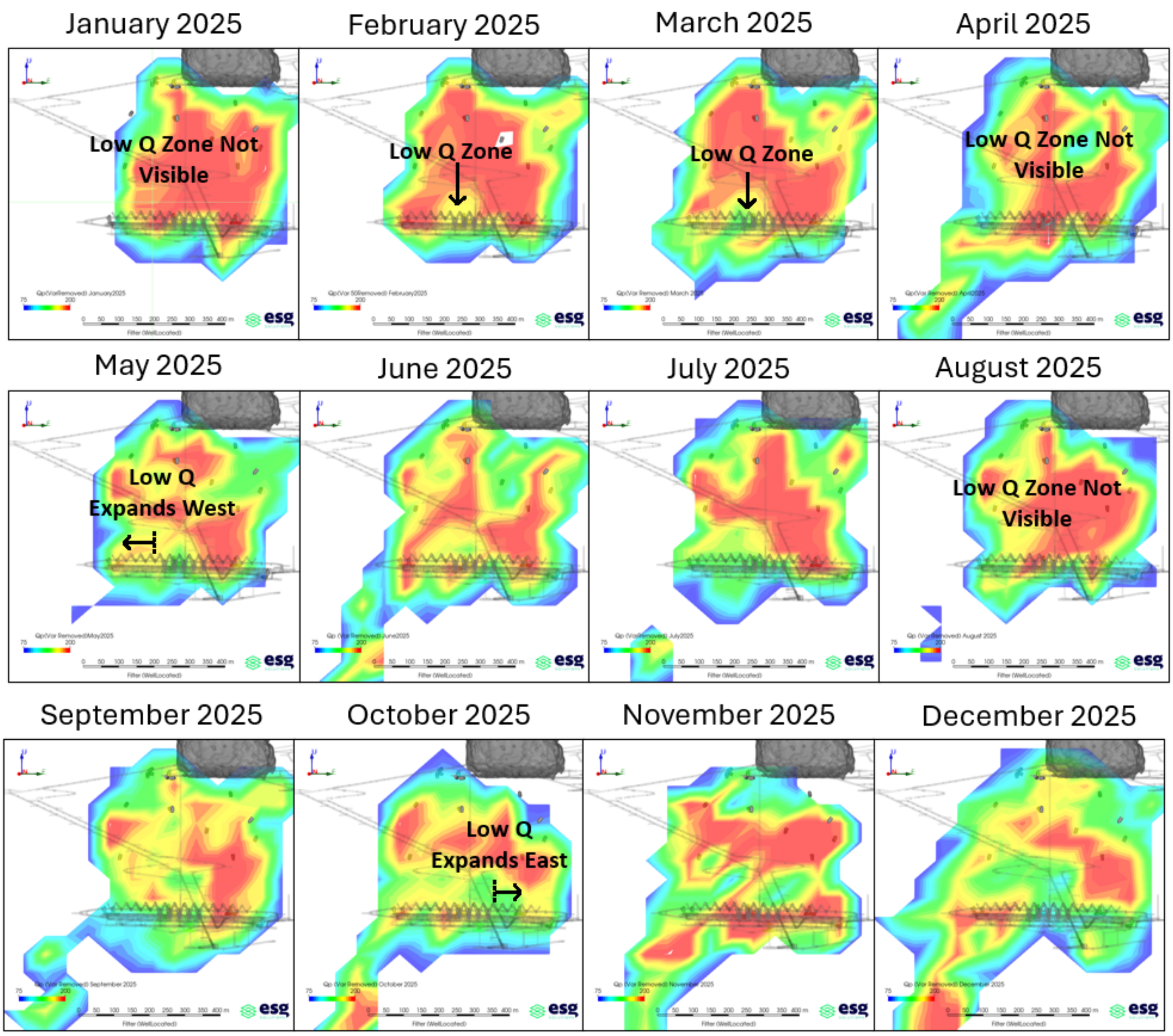

Figure 8 Qp attenuation field at monthly intervals from January to December 2025. The cutting plane is the same as shown for the velocity tomography results in Figure 6

Figure 9a shows a close-up of the December attenuation tomography field along with the December seismicity above the C-Zone and the conservative estimate of the cave shape from Geo4Sight. This result shows that the seismogenic zone above the cave displays higher Q. Similar to velocity tomography, the lower Q zone appears to extend further than the estimated cave shape on the west side, indicating that the rock mass may be damaged or have a different composition compared to the surrounding rock.

For completeness, Figure 9b shows the change in Qp field from January to December 2025. This field is sparse compared to the velocity difference field. The seismogenic zone is occurring in an area with lower Q (a change of −30 to −90) compared to January. This is consistent with the seismicity occurring within intact rock mass that is beginning to yield.

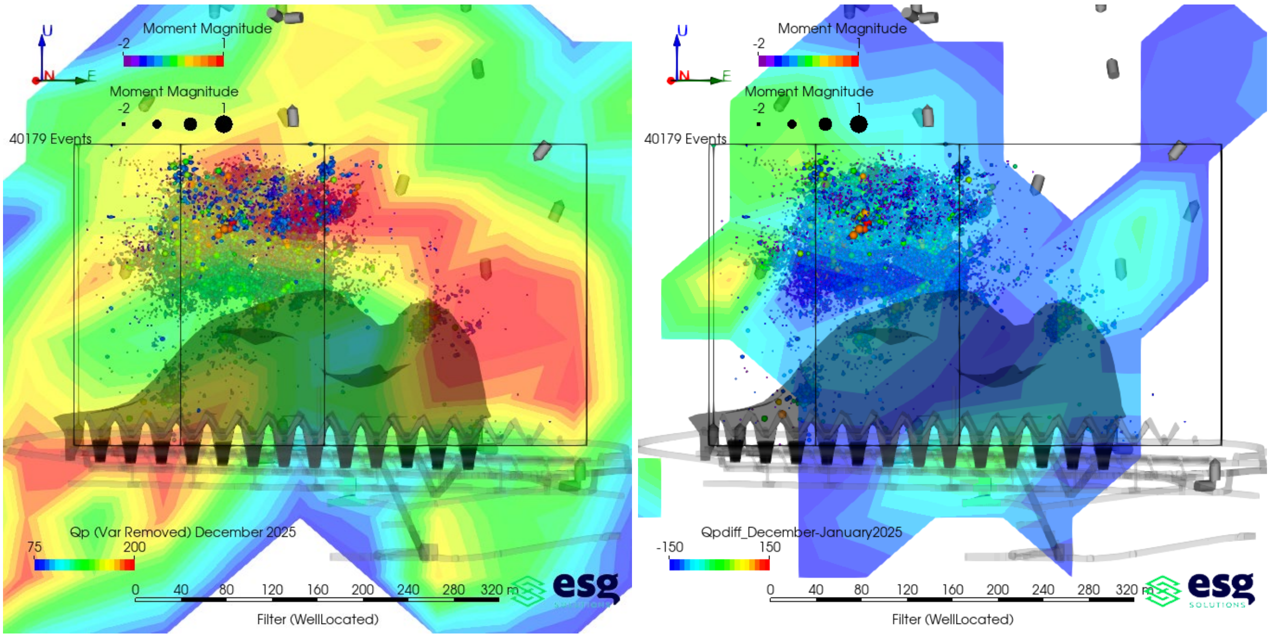

(a) (b)

Figure 9 (a) Qp attenuation field for December 2025; (b) Qp attenuation difference field showing the change in attenuation from January to December 2025. An estimated cave shape from Geo4Sight obtained at the start of January 2026 and the December 2025 seismicity above the C-Zone are superimposed on these images

4 Conclusion

P-wave velocity and attenuation (Qp) tomography were used to image the development and progression of the C-Zone cave at the New Afton mine. Both methods provide additional insight into the rock mass than the seismicity alone would. Attenuation tomography was compared to the more traditional travel-time tomography results and showed similar trends, with low attenuation zones consistent with low velocity zones and both occurring where cave propagation was expected. Some challenges were observed with attenuation tomography, where higher uncertainty was present in the attenuation estimates compared to the velocity estimates for volumes with the same number of ray paths. This resulted in a smaller usable tomographic field for comparison with the velocity field. The higher uncertainty may be attributed to the nature of the method, which requires use of the full waveform spectral data and is therefore more sensitive to signal quality limitations in the available sensors, as well as other sources of attenuation such as reflection and diffraction of the P-waves. Future analysis could help reduce some of these uncertainties by applying the observed velocity field to the ray path assumption prior to performing attenuation tomography.

Comparison of the 2 tomographic methods suggests a potential advantage of attenuation tomography over travel-time tomography, as growth of the low Q zones appeared to precede development of the low velocity zones. This may indicate that attenuation is more sensitive to changes in the rock mass and is capable of detecting those changes earlier than they are expressed in the velocity field.

Acknowledgement

The authors thank Coeur Mining and New Afton for permission to use and show their data. The views and opinions presented in the article are the authors' own and do not reflect any position or outlook of Coeur New Afton.

References

Barthwal, H, Calixto, FJ & van der Baan, M 2019, '3-D attenuation tomography from microseismicity in a mine', *Geophysical Journal International*, vol. 219, no. 3, pp. 1805–1817, https://doi.org/10.1093/gji/ggz396

Brune, JN 1970, 'Tectonic stress and the spectra of seismic shear waves from earthquakes', *Journal of Geophysical Research*, vol. 75, no. 26, pp. 4997–5009, https://doi.org/10.1029/JB075i026p04997

Crowley, JW, Baig, AM, Urbancic, T & von Lunen, E 2015, '4D tomography and deformation from microseismic data', *Proceedings of the SEG Technical Program Expanded Abstracts 2015*, pp. 2537–2541, https://doi.org/10.1190/segam2015-5906861.1

Eberhart-Phillips, D. & Chadwick, M. 2002, 'Three-dimensional attenuation model of the shallow Hikurangi subduction zone in the Raukumara Peninsula, New Zealand', *New Zealand Journal of Geophysical Research*, vol. 102, no. B2, https://doi.org/10.1029/2000JB000046

Kamp, C, Conley, A, Collins, DS, Preiksaitis, M, Butler, T & Shumila, V 2022, 'Use of seismic tomography to aid rock mechanics interpretation at New Afton B3 block cave mine', in Y Potvin (ed.), *Caving 2022: Proceedings of the Fifth International Conference on Block and Sublevel Caving*, Australian Centre for Geomechanics, Perth, pp. 461–472, https://doi.org/10.36487/ACG_repo/2205_31

Krauß, F, Giese, R, Alexandrakis, C & Buske, S 2014, 'Seismic travel-time and attenuation tomography to characterize the excavation damaged zone and the surrounding rock mass of a newly excavated ramp and chamber', *International Journal of Rock Mechanics and Mining Sciences*, vol. 70, pp. 524–532, https://doi.org/10.1016/j.ijrmms.2014.06.010

New Gold Inc. 2020, *Technical Report on the New Afton Mine, British Columbia, Canada (NI 43-101 Report)*, Kamloops.

Nizkous, I, Smith-Boughner, L, Shumila, V, de Beer, W & Angus, D 2020, 'Multi-attribute microseismic analysis to evaluate the evolution of in situ stress: imaging the complex relationship between stress and structure', *MassMin 2020: Proceedings of the Eighth International Conference & Exhibition on Mass Mining*, pp. 1268–176, https://doi.org/10.36487/ACG_repo/2063_94

Nur, A & Simmons, G 1969, 'The effect of saturation on velocity in low porosity rocks', *Earth and Planetary Science Letters*, vol. 7, no. 2, pp. 183–193, https://doi.org/10.1016/0012-821X(69)90035-1

Rietbrock, A 2001, 'P wave attenuation structure in the fault area of the 1995 Kobe earthquake', *4154*, vol. 106, no. B3, pp. 4141, https://doi.org/10.1029/2000JB900234

Romero, AE, McEvilly, TV & Majer, EL 1997, '3-D microearthquake attenuation tomography at the Northwest Geysers geothermal region', *Geophysics* , vol. 62, no. 1, pp. 149–167, https://doi.org/10.1190/1.1444114

Scherbaum, F 1990, 'Combined inversion for the three-dimensional Q structure and source parameters using microearthquake spectra', *Journal of Geophysical Research: Solid Earth*, vol. 95, no. B8, pp. 12423–12438, https://doi.org/10.1029/JB095iB08p12423

Watanabe, T & Sassa, K 1996, 'Seismic attenuation tomography and its application to rock mass evaluation', *International Journal of Rock Mechanics and Mining Sciences & Geomechanics Abstracts*, vol. 33, no. 5, pp. 467–477, https://doi.org/10.1016/0148-9062(96)00005-8